MATERIALS SCIENCE

Prolate and oblate chiral liquid crystal spheroids

Monirosadat Sadati[1,2], Jose A. Martinez-Gonzalez[1,3], Ye Zhou[1], Nader Taheri Qazvini[1,2], Khia Kurtenbach[1], Xiao Li[1,4], Emre Bukusoglu[5], Rui Zhang[1], Nicholas L. Abbott[6], Juan Pablo Hernandez-Ortiz[7], Juan J. de Pablo[1,8]*

Liquid crystals are known to exhibit intriguing textures and color patterns, with applications in display and optical technologies. This work focuses on chiral materials and examines the palette of morphologies that arises when microdroplets are deformed into nonspherical shapes in a controllable manner. Specifically, geometrical confinement and mechanical strain are used to manipulate orientational order, phase transitions, and topological defects that arise in chiral liquid crystal droplets. Inspired by processes encountered in nature, where insects and animals often rely on strain and temperature to alter the optical appearance of dispersed liquid crystalline elements, chiral droplets are dispersed in polymer films and deformation induced by uniaxial or biaxial stretching. Our measurements are interpreted by resorting to simulations of the corresponding systems, thereby providing an in-depth understanding of the morphologies that arise in these materials. The reported structures and assemblies offer potential for applications in smart coatings, smart fabrics, and wearable sensors.

INTRODUCTION

Liquid crystals (LCs) exhibit ordered mesophases that arise from anisotropic molecular shapes and packing considerations. They represent a unique class of oil-based synthetic materials with tunable long-range orientation and have found a wide range of applications, from display technologies and optical devices to chemical and biomolecular sensors (*1*–*8*). In the nematic phase, LC molecules tend to align along a uniform direction, the so-called director $\hat{\mathbf{n}}$. Chiral structures can be induced in nematic LCs by adding a chiral dopant, which makes the average director twist in the direction perpendicular to the molecular axis. In a chiral nematic, or cholesteric phase, the periodicity of the helical structure is described by the pitch (p), which is the distance corresponding to a 2π rotation of the molecular orientation (director n). Cholesteric LCs with a self-organized helical structure exhibit specific reflection patterns that originate from that structure (*9*) and are considered attractive candidates for a wide range of photonic applications (*10*, *11*). According to Bragg's law $\lambda = np$, the wavelength of the reflected light λ is attributed to the product of the average refractive index (n) of the LC and the with pitch length (p). The color change of a cholesteric LC can be controlled by adjusting the cholesteric pitch p, through the chiral dopant concentration, temperature, thickness of the confinement, electric fields, and laser light (*12*). The higher the dopant concentration or temperature, the shorter the helical pitch becomes, thereby shifting the reflected light to shorter wavelengths (*13*). At high dopant concentrations or chirality, the blue phase structures (BPI and BPII) emerge between the cholesteric and isotropic phases. They exhibit cuboidal lattice structures stabilized by line defects and are capable of undergoing lattice transformations that occur through a martensitic-like process (*14*, *15*). Blue phases (BPs) are particularly interesting in that they show highly selective reflection of incident light and submillisecond response times (*16*, *17*).

A growing interest in the integration of chiral LCs into devices, such as fiber optics or wearable sensors, requires an understanding of the interplay between spatial restrictions, curvature, and ordering associated with this class of liquid crystalline materials. Computational simulations have recently shown that confining chiral LCs into channels can alter their defect structures and endow them with supramolecular configurations and rich defect topologies (*18*–*26*). The frustration of chiral LC molecules in curved geometries has been shown to have a substantial effect on their alignment and self-organization (*21*, *23*, *25*). Chiral LCs confined in spherical droplets (*12*, *27*–*34*) exhibit defect structures that arise from the interplay of the inherent twist configuration of a chiral LC and the curvature of a spherical cavity; the p/R ratio, where p and R are the pitch of the cholesteric and the radius of the sphere droplet, respectively, determines the particular configuration that one may encounter. Recently, through a combination of theory and experiment, Zhou *et al.* (*32*) reported that increasing the chirality of LCs confined into micrometer-sized droplets can lead to a continuous transition from a twisted bipolar structure to a radial spherical structure. This finding has been attributed to the balance between LC elasticity, chirality, and surface energy that occurs in a confined geometry. Moreover, they demonstrated that nanoparticles are localized at the defect regions on the surface of the droplets in a manner that is dictated by the configuration of the underlying chiral LC (*32*, *33*). Bagnani *et al.* (*35*) have reported the emergence of different configurations, including homogeneous, radial, bipolar, radial chiral, and uniaxial chiral nematic in cholesteric amyloid fibrils tactoids. Bukusoglu *et al.* (*36*) studied BPI and BPII in droplets dispersed in water. They used experiments and theory to show that blue phase liquid crystals (BPLCs) confined into a sphere strain the cubic lattice structures near the interface, thereby altering the Bragg diffraction and inducing the formation of a monodomain BP (*36*). Computational studies by Martínez-González *et al.* (*21*) have also shown that confining a BPLC into a small droplet can influence the structure of defects and the stability of the corresponding phases.

[1]Pritzker School of Molecular Engineering, University of Chicago, Chicago, IL 60637, USA. [2]Department of Chemical Engineering, Swearingen Engineering Center, University of South Carolina, Columbia, SC 29208, USA. [3]Facultad de Ciencias, Universidad Autónoma de San Luis Potosí, Av. Parque Chapultepec 1570, San Luis Potosí 78295, SLP, México. [4]Department of Materials Science and Engineering, University of North Texas, Denton, TX 76203, USA. [5]Chemical Engineering Department, Middle East Technical University, Ankara 06800, Turkey. [6]Smith School of Chemical and Biomolecular Engineering, Cornell University, Ithaca, NY 14853, USA.. [7]Departamento de Materiales y Minerales, Facultad de Minas, Universidad Nacional de Colombia, Sede Medellín, Calle 75 # 79A-51, Bloque M17, Medellín, Colombia. [8]Argonne National Laboratory, 9700 Cass Avenue, Lemont, IL 60439, USA.
*Corresponding author. Email: depablo@uchicago.edu

Recently, Palacio-Betancur *et al.* used simulations to explore the configuration of BP droplets under multiaxial deformation. Their results indicate that, in oblate cavities, cuboidal BP structures transform into half skyrmions, and the geometrical constraints induced by the prolate spheroidal shape lead to hybridization of the BPs (*37*).

Building on past studies in spherical droplets, core-shell geometries have now been used to explore the effects of curvature on the molecular configuration and optical properties of chiral LCs. When a chiral LC is confined into a shell, a new structure appears, where large stripes engulf focal conic domains and small, perpendicularly aligned substripes (*38*–*40*). By taking advantage of the selective reflection property of chiral LCs, Lee *et al.* (*41*–*45*) have managed to design photonic microcapsules that rely on confinement into core and shell geometries, where the spherical symmetry provides rotation-independent photonic properties. Fialho *et al.* (*46*) have computationally explored the effect of curvature on the alignment of a cholesteric LC in different geometries, including cylindrical walls and pores as well as toroidal domains. They have shown that curvature-induced stresses can alter molecular alignment and distort periodicity. In addition, a symmetry breaking behavior of cholesteric layers has been reported for toroidal geometries (*46*). In parallel studies, Wand *et al.* (*47*) have examined the effect of confinement in torus-shaped and cylindrical domains using Monte Carlo simulations. They found that confining a chiral LC in a cylindrical cavity with planar anchoring leads to a defect-free domain with a twisted director field. In toroidal domains with homeotropic surface anchoring, an unstable twisted configuration appears in the form of a single disclination line or a pair of intertwined disclination rings with knotted defect structures (*47*).

As the summary above illustrates, past studies have focused on stationary confinement of LCs in spherical droplets. The work reported here focuses on the continuous and reversible deformation of confined cholesteric LCs into oblate and prolate domains, and it offers access to a rich palette of optically active structures that had not been considered before. By relying on both experiments and computational simulations, we demonstrate that the coupling of curvature, elasticity, and strain of the chiral LC leads to the emergence of new, stable molecular configurations with potential applications as mechano-optical meta materials in smart coatings, wearable electronics, and sensors.

MATERIALS AND METHODS

The mesogen MLC 2142 and the chiral dopant 4-(1-methylheptyloxycarbonyl) phenyl-4-hexyloxybenzoate (S-811) were purchased from Merck (the molecular structure of S-811 is shown in Fig. 1A). Poly vinyl alcohol (PVA, average M_w = 85k to 124k, 87 to 89% hydrolyzed) and poly acrylic acid (PAA, M_w = 100k) were purchased from Sigma-Aldrich. All materials were used as received. The 6 and 35 wt % of S-811 in MLC 2142 mixtures were prepared using toluene as a cosolvent and incubated at room temperature overnight. Toluene was then evaporated using a rotary evaporator at 50°C. Chiral LC droplets were prepared by emulsifying 10 μl of mixtures in 2 ml of mQ water using a Branson 450 Sonifier at 20% output power with a 3-mm tip. Immediately after, the PVA solution (or PAA solution) was added to the emulsion to stabilize the system (Fig. 1B). PVA and PAA are both water-soluble polymers; they are immiscible with the LC and ensure strong planar anchoring at the surface of chiral LC droplets. The final polymer concentration in the emulsion was 10 wt %. The emulsion was plasticized with glycerol (1 wt %) and casted on a glass substrate and dried at 30°C for 2 days. After water evaporation, the polymer film was cut into rectangular stripes with dimensions of 10 mm by 30 mm and carefully peeled off from the glass substrate. The polymer thickness was measured to be 100 to 120 μm, and the LC concentration in the dried polymer film was 5 wt %. To deform chiral LC droplets, a polymer-dispersed LC (PDLC) film was mounted on a manual tensile machine (Micro Vice Holder, STJ-0116-A, S.T. Japan Inc.), which can stretch the film uniaxially using two micrometer screw gauges (fig. S1). The extension was increased in a stepwise manner, and the reflection band was measured using a Flame VIS-NIR Miniature Spectrometer ($\lambda > 350$ nm). We used an Olympus BX51 optical microscope equipped with cross polarizers to monitor changes in shape, configuration, and optical properties of the droplets before and during deformation of the PDLC film.

At a theoretical level, a continuum mean field Landau-de Gennes formalism (*48*–*51*) was adopted to describe the liquid crystalline system. In this formalism, the free energy of the LC, F, is modeled in terms of the tensor order parameter, $\boldsymbol{Q}$, defined by $Q_{ij} = S\,(n_i\, n_j - 1/3\,\delta_{ij})$, with $i, j = 1, 2, 3$, and n_i are the x, y, and z components of the local director vector and S is the scalar order parameter. The free energy functional is given by

$$F(\boldsymbol{Q}) = \int \mathrm{d}^3 x\,[f_P(\boldsymbol{Q}) + f_E(\boldsymbol{Q})] + \int \mathrm{d}^2 x f_S(\boldsymbol{Q}) \tag{1}$$

where the short-range contribution, f_P, is given by

$$f_P = \frac{A}{2}\left(1 - \frac{U}{3}\right)\mathrm{tr}(\boldsymbol{Q}^2) - \frac{AU}{3}\mathrm{tr}(\boldsymbol{Q}^3) + \frac{AU}{4}\mathrm{tr}(\boldsymbol{Q}^2)^2 \tag{2}$$

In Eq. 2, A and U are phenomenological parameters that depend on temperature and pressure. The elastic free energy is given by

$$f_E = \frac{1}{2}\left[L\frac{\partial Q_{ij}}{\partial x_k}\frac{\partial Q_{ij}}{\partial x_k} + 2Lq_0\epsilon_{ikl}Q_{ij}\frac{\partial Q_{lj}}{\partial x_k}\right] \tag{3}$$

where $q_0 = 2\pi/p$ is the inverse of the pitch (p), L is an elastic constant, and ϵ_{ikl} is the Levi-Civita tensor. The last term of Eq. 1 corresponds to the surface contributions to the free energy. For planar degenerate anchoring, we have (*44*)

$$f_S^P = W_P(\widetilde{\boldsymbol{Q}} - \widetilde{\boldsymbol{Q}}^{\perp})^2 \tag{4}$$

where W_P is the anchoring energy, $\widetilde{\boldsymbol{Q}} = \boldsymbol{Q} + S\boldsymbol{I}/3$, and $\widetilde{\boldsymbol{Q}}^{\perp} = \boldsymbol{P}\widetilde{\boldsymbol{Q}}\boldsymbol{P}$. The projection operator is defined by $P_{ij} = \delta_{ij} - \nu_i\nu_j$, where $\boldsymbol{\nu}$ is the vector normal to the surface.

Minimization of the free energy, which leads to metastable and stable states, was achieved using a Ginzburg-Landau relaxation method where $\boldsymbol{Q}$ evolves toward equilibrium according to (*49*, *50*)

$$\frac{\partial \boldsymbol{Q}}{\partial t} = -\frac{1}{\gamma}\boldsymbol{\Pi}\left(\frac{\delta F}{\delta \boldsymbol{Q}}\right) \tag{5}$$

with boundary conditions such that $\boldsymbol{\Pi}[(\delta F/\delta\,\nabla\,\boldsymbol{Q})\cdot\boldsymbol{\nu}] = 0$, where $\boldsymbol{\Pi}(\boldsymbol{B}) = 1/2\,(\boldsymbol{B} + \boldsymbol{B}^{\mathrm{T}}) - 1/3\,\mathrm{tr}(\boldsymbol{B})\,\boldsymbol{I}$ ensures the symmetric and traceless

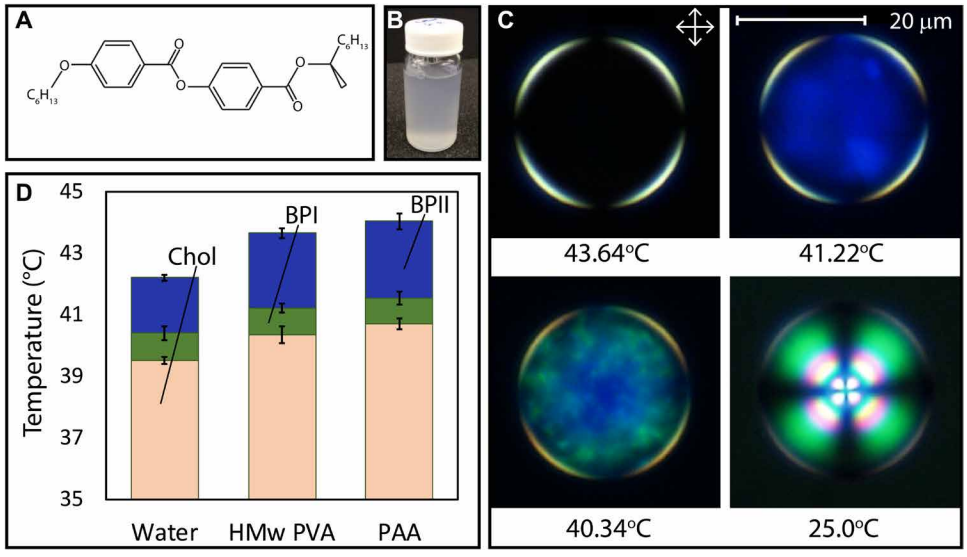

Fig. 1. Phase transitions of high-chirality LC droplets in aqueous polymer solutions. (**A**) Molecular structure of the chiral dopant, S-811; (**B**) chiral LC droplets (MLC 2142 and 36.25 wt % S-811) dispersed in 10 wt % PVA aqueous solution. (**C**) Cross-polarized reflection mode micrographs presenting phase transitions of a 25-μm chiral LC droplet in 10 wt % high-molecular weight (HMw) PVA solution cooled from the isotropic phase at 0.2°C/min. (**D**) Effect of polymer type on the phase-transition temperatures of chiral LC droplets [MLC 2142/S-811 63.75/36.25 (wt %)] dispersed in aqueous solutions (Chol, cholesteric (chiral); BPI, blue phase I; and BPII, blue phase II). Photo credit: Monirosadat Sadati, The University of Chicago.

properties of the $\boldsymbol{Q}$-tensor parameter and γ is a diffusion coefficient. Initial configurations for BPI were generated according to (*48*, *49*, *51*)

$$Q_{xx} = a(-\sin(ky/\sqrt{2})\cos(kx/\sqrt{2}) - \sin(kx/\sqrt{2})\cos(kz/\sqrt{2}) + 2\sin(kz/\sqrt{2})\cos(ky/\sqrt{2})) \quad (6)$$

$$Q_{xy} = a(-\sqrt{2}\sin(kx/\sqrt{2})\sin(kz/\sqrt{2}) - \sqrt{2}\cos(ky/\sqrt{2})\cos(kz/\sqrt{2}) + \sin(kx/\sqrt{2})\cos(ky/\sqrt{2})) \quad (7)$$

For BPII, we used

$$Q_{xx} = a(\cos kz - \cos ky) \quad (8)$$

$$Q_{xy} = a \sin kz \quad (9)$$

where the amplitude of initialization is $a = 0.2$, the strength of the chirality is given by $k = 2q_0 r$, and r is the red shift, which was found to be 0.71 for BPI and 0.86 for BPII (*21*). In all cases, the components *yy*, *zz*, *xz*, and *yz* were obtained by cyclic permutation of those given above. The BP lattice parameters a_{BPI} and a_{BPII} are given by $a_{BPI} = \frac{p}{\sqrt{2}r}$, $a_{BPII} = \frac{p}{2r}$. For the cholesteric phase, different initial configurations were used, including random, uniform, helical, a radial spherical configuration (RSS) (*52*), and a radial ellipsoidal configuration deformed from RSS according to the aspect ratio of the system geometry.

For the description of the system, we used a finite difference method with a mesh resolution of 7.15 nm and strong anchoring, $W_P = 1 \times 10^{-3}$ J/m^2; $A = 1.067 \times 10^5$ J/m^3, $L = 6$ pN, chiral pitch $p = 258$ nm, and thermal parameter $U = 2.755$ for BPII, $U = 3.0$ for BPI, and $U = 5.0$ for the cholesteric phase. These values are found to be consistent with experimental results (*21*, *36*). BP topological defects were visualized through isosurfaces of the scalar order parameter of $S = 0.35$ for BPII and $S = 0.42$ for BPI.

The polarized light micrographs were calculated using the Jones matrix formalism, in which light traverses along a chosen direction and the total phase shift is accumulated. A wavelength of 350 nm was sufficient to solve the structural details of the observed morphologies.

RESULTS AND DISCUSSION

The optical properties of the chiral LC droplets (diameters of 10 to 30 μm) were first investigated in PVA and PAA solutions (Fig. 1, C and D). Figure 1C shows the optical appearance of a 25-μm high-chirality LC droplet in the reflection mode of a cross-polarizer in PVA solution during cooling from 50° to 25°C at 0.2°C min^{-1}. At high concentrations of the chiral dopant (S-811), the BP structures emerge between the isotropic and cholesteric phases (Fig. 1C) (*14*, *36*). Upon cooling from the isotropic phase, BPII domains reflecting blue light nucleate and grow as the temperature decreases. By further decreasing the temperature, the BPII with its simple cubic lattice structure transitions into a BPI, which has a body-centered cubic lattice structure, and can be identified by the appearance of a green color. This color change is attributed to an increase in the helical pitch length when cooling the sample. We compared the effect of PVA and PAA polymers on the temperature-dependent optical properties of the BPLC droplets to those of a pure water–LC emulsion (Fig. 1D). Our measurements reveal a significant increase in the absolute value of the transition temperatures (Iso-BPII-BPI-Chol) of the BPLC droplets dispersed in PVA or PAA polymer solutions compared to those in pure water. PVA and PAA raise the BP transition temperatures by 0.7° and 1.2°C, respectively. Moreover, PVA and PAA enlarge the stability range of BPII by about 33% with respect to that observed in pure water (Fig. 1D).

Oblate chiral LC droplets were formed by a slow drying process of the PDLC solution on a glass substrate. When water evaporates,

the polymer film shrinks to a level that can be controlled by the initial polymer solution, including type and concentration. This process leads to a geometrical deformation of the LC droplets, from spherical to oblate. The cross section of the polymer film was examined by *s*canning electron microscopy (SEM) to determine the level of deformation of the chiral LC droplets (Fig. 2, A and B). Cross sections were prepared by breaking the polymer film after freezing in liquid nitrogen.

Cross-polarized reflection mode micrographs of the chiral LC droplets embedded in a dry PVA film show that geometrical deformation divides the chiral LC droplet into two separate regions with distinct LC molecular alignment. The outer part maintains the structure of the spherical droplet, with its RSS rings. However, the inner part adopts a disc-shape topology, where the strong planar anchoring forces the randomly oriented helical axis within the droplet to adopt a uniform alignment normal to the surface so that the director aligns tangential to the surface. The flat planar region of the now oblate chiral LC drop selectively reflects light of the color corresponding to the pitch length (*53*). Therefore, a chiral LC with higher dopant concentration and shorter pitch length reflects light at blue wavelengths, while the reflectance spectra of the LC with low dopant concentrations occurs at larger wavelengths (Fig. 2, D and I).

Our simulation results show that when a LC with low or high chirality is confined into an oblate spheroid, the concentric twisting layers of the RSS expand biaxially, and a domain of cholesteric phase emerges between the flattened surfaces along the *z* axis (Fig. 2, E and F) (see simulation results for the low-chirality LC oblate drop). Consistent with our experimental observations, these helical layers lead to a bright circle in the center of the cross-polarized image in the top view (Fig. 2, E and F). Moreover, the RSS in the spherical droplet transforms into a more complicated configuration, with disclination lines forming inside (Fig. 2, G and H). Due to compression along the *z* axis, the double helix of bend distortions in RSS (*28*) breaks into two spiral-shape disclination lines (yellow in Fig. 2G). On the other hand, when the LC is confined into large oblate spheroids ($D_x = D_y$), we obtain a diametrical oblate structure (DOS) for high chirality (p = 258 nm) that resembles the diametrical spherical structure (DSS) (*54*). In addition to the characteristic ring defects of the DSS (a series of single unlinked loops in the diametrical region), the DOS configuration exhibits other

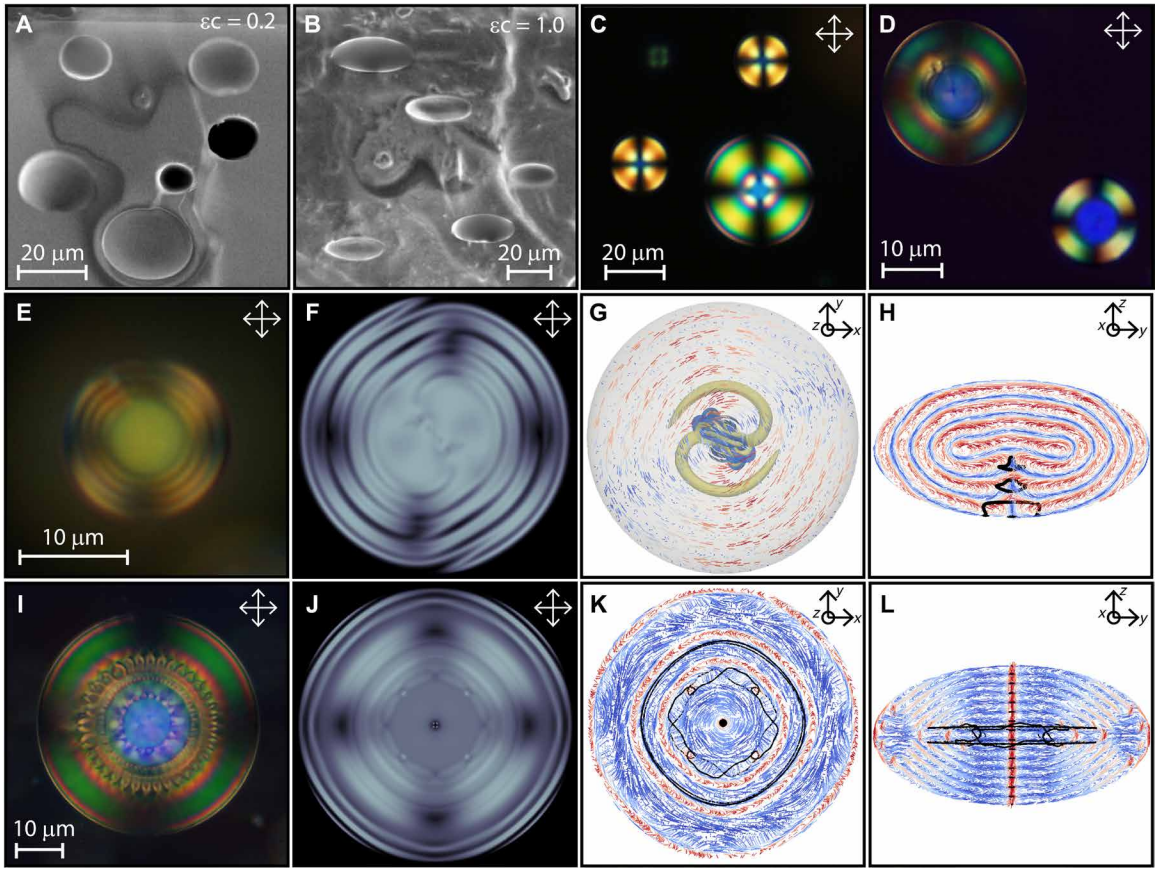

Fig. 2. Chiral LC droplets embedded in polymer films. (**A** and **B**) SEM micrographs of the cross section (side view) of high-chirality LC droplets embedded in dry PAA and PVA films, respectively. (**C** and **D**) Polarized optical microscopy (POM) of high-chirality LC droplets embedded in dry PAA and PVA films, respectively. (**E**) POM of a low-chirality LC droplet (6 wt % chiral dopant, $N = 5$) in a dry PVA film. (**F**) POM and (**G** and **H**) directors obtained from simulations for a low-chirality nematic oblate with $D_x = D_y = 4$ μm, $D_z = 2$ μm and pitch = 630 nm (colors are from blue to red according to $\hat{n} \cdot \hat{z}$). The splay and bend elastic distortions are shown in blue ($S_{SB} > 0.002$) and in yellow ($S_{SB} < -0.002$), respectively. Defects are shown in black (isosurface for $S = 0.5$). (**I**) POM of a 60-μm high-chirality LC droplet in dry PVA films. (**J** and **K**) POM, directors, and defects from simulations for a nematic oblate with $D_x = D_y = 4$ μm, $D_z = 2$ μm and pitch = 258 nm. (H) and (**L**) represent side views of the directors along the *y* axis. (C) to (F), (I), and (J) are taken in the *xy* plane.

topological line defects, which produce knots that have been identified as a four-component link in the central region [according to the Rolfsen table (*55*), it corresponds to N_j^k, where the crossing number is $N = 8$, the number of blades is $k = 4$, and the order number is $j = 1$], followed by two single unlinked loops in the outer part (fig. S2). The four-component link exhibits a curly appearance in the simulated cross-polarizer images (Fig. 2K), which has also been observed in our experiments (Fig. 2I). This emerging, distinct morphology can be attributed to the effect of confinement size on the phase transition temperatures (*36*).

To further investigate the effect of confinement shape and curvature on the molecular organization of chiral LCs, we uniaxially stretched the PDLC film. Systematic deformation of the droplets from their original spherical or oblate geometry by stretching of the PDLC samples was carried out under an optical microscope. Our cross-polarized images show that the LC droplets form ellipsoidal shapes that are aligned with their major axes along the stretching direction. Our cross-polarized micrographs demonstrate that the uniaxial stretching of the chiral LC droplets destabilizes the RSS configuration. RSS rings disappear from the center outward (Fig. 3A and movie S1) as strain is increased. The strain values are defined as $\varepsilon = (L - L_o)/L_o$, where L_o is the initial diameter of the droplet and L represents the long axis of the ellipsoidal droplet at a given strain. Moreover, a pronounced color change accompanies the stretching of the chiral LC droplets, which we evaluate by visual observation during stretching and measure spectroscopically (fig. S3). According to the spectroscopy results, increasing strain shifts the reflection band of the frustrated chiral LC toward a lower wavelength (fig. S3), producing a color change from orange to green. When the film was unloaded, the orange color of the LC droplet was restored (fig. S4).

To expand on this phenomenon, we performed simulations of ellipsoidal cavities with various aspect ratios and explored the possible configurations. Our simulation results indicate that in the early stages of the uniaxial stretching along the x axis, the configuration is still RSS-like with concentrically twisting layers near the boundary of the ellipsoidal cavity and uniaxially twisting structure in the center with helical axis along the z axis. As the oblate is stretched further ($D_x = 3D_y$, where D_x and D_y are axes diameters in the x and y directions, respectively), the high curvature near the ellipsoid ends in the x axis and the strong confinement along the z axis drives the most inner twisting layer toward the center and the RSS-like structure becomes destabilized. From $D_x = 3D_y$ (Fig. 3), the helical structure under ellipsoidal confinement becomes energetically more favorable than the RSS-like structure.

The optical properties of the LC in the ellipsoidal cavities of the stretched polymer films were further investigated for the high-chirality LC sample. Similar to the low-chirality LC, cross-polarized micrographs of the high-chirality LC droplets show that the RSS rings disappear under uniaxial deformation (Fig. 4, A and B, and movie S2). However, due to the high chirality of the LC, it is difficult to discern individual RSS rings. Figure 4 (A and B) shows the cross-polarized micrographs of the oblate chiral LC droplets before and after deformation at room temperature. Upon uniaxial stretching, we observe a pronounced color change from brownish-orange to deep blue (Fig. 4, A and B). Diffused reflection spectra before and after stretching the sample are shown in Fig. 4 (A and B). The color change is gradually restored after releasing the strain (fig. S4). The remaining deformation in the unloaded sample can be attributed to the residual plastic deformation of the polymer film, which did not allow a full recovery to the initial length.

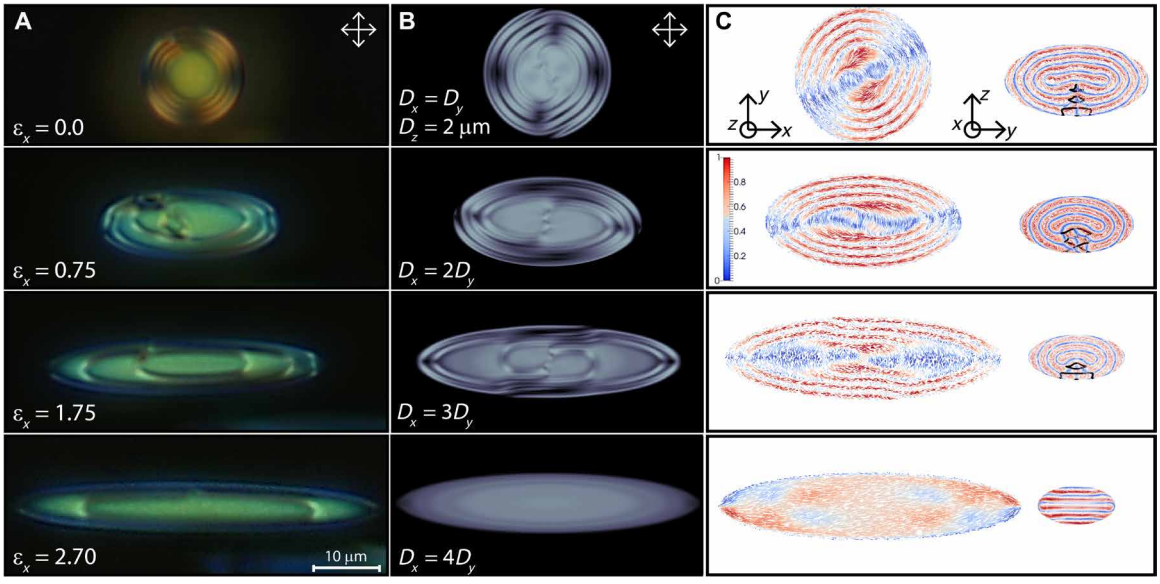

Fig. 3. Transformation of the RSS structure to the helical configuration upon uniaxial deformation. (**A**) Cross-polarized reflection mode micrographs of a uniaxially stretched low-chirality LC oblate ($N = 5$) droplet embedded in a dry high–molecular weight PVA film. (**B**) Polarized light micrographs and (C) director fields obtained from simulations for chiral nematic ellipsoids with pitch = 630 nm during uniaxial stretch along the x axis. The axis lengths for the ellipsoids from top to bottom are $D_x = D_y = 4\ \mu m$, $D_z = 2\ \mu m$; $D_x = 2D_y$, $D_z = 1.59\ \mu m$; $D_x = 3D_y$, $D_z = 1.39\ \mu m$; and $D_x = 4D_y$, $D_z = 1.287\ \mu m$, respectively. The RSS-like structure becomes destabilized upon uniaxial deformation of the oblate, and a helical configuration becomes energetically more favorable from $D_x = 3D_y$. First and last columns in panel (**C**) represent the top view and side view of the director fields, receptively. The director field is colored according to its projection on the x axis. Defects are shown in black (isosurface for $S = 0.5$). The experimental and simulated cross-polarized micrographs presented in images (A) and (B) are taken in the xy plane.

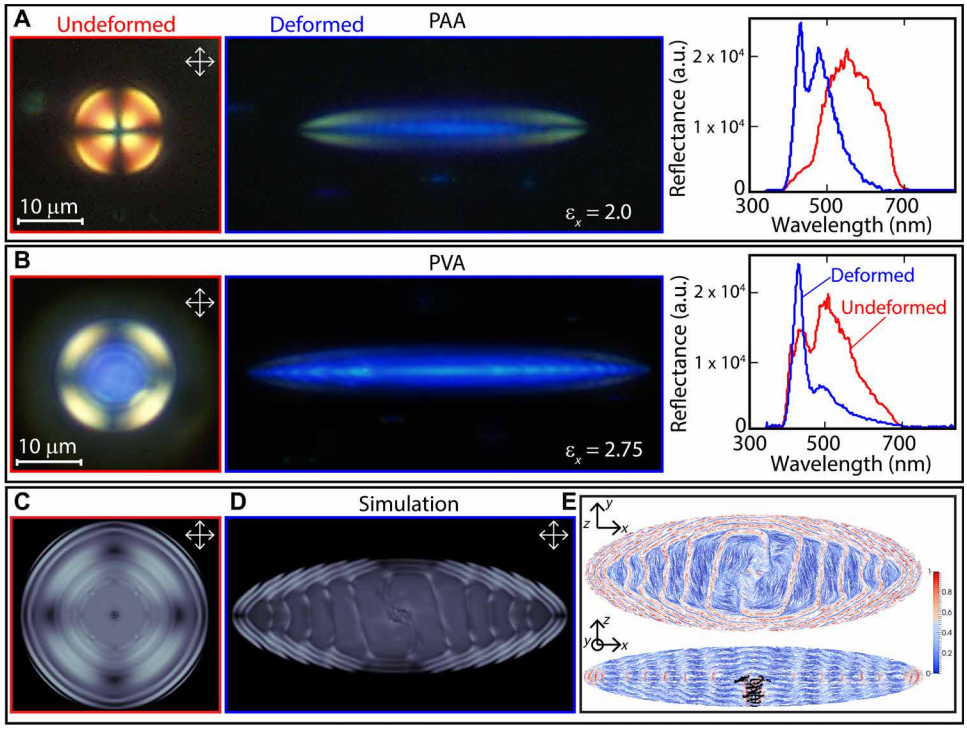

Fig. 4. Uniaxial deformation of the high-chirality LC destabilizes the RSS structure and shifts the light of the reflection band to shorter wavelengths. (**A**) Cross-polarized reflection mode micrographs and the reflectance spectra of a high-chirality LC sphere droplet embedded in a PAA polymer film before and after strain ($\varepsilon = 2.0$). a.u., arbitrary units. (**B**) Cross-polarized reflection mode micrographs and the reflectance spectra of a high-chirality LC oblate embedded in a PVA polymer film before and after strain ($\varepsilon = 2.75$). (**C** and **D**) Cross-polarized images of the high-chirality LC confined in an oblate and uniaxially stretched droplet obtained by simulations. (**E**) Top and side view (with defect line) of the director field configuration along the *x* axis. Director is colored based on its projection onto the *z* axis, and the order parameter defect lines (black) correspond to $S = 0.6$. Blue regions correspond to a director alignment on the *xy* plane; near the border, the director field shows the typical cholesteric behavior (deformed RSS).

In the past few years, mechanically responsive chiral LCs have attracted considerable attention for sensing applications. In chiral LC elastomers, or a high-viscosity chiral LC sandwiched between polymer films, deformation-induced color change is attributed to a reduction in helix length due to a decrease in the film thickness upon straining (*56*–*60*).

Stretching of the polymer-dispersed chiral LC films leads to contraction along the axis normal to the surface of the film. Since the volume of the LC does not change, the extension of the polymer film results in a reduction in the size of the droplet along the *z* axis, which may cause a change in the pitch length of the chiral LC and the subsequent color shift.

We further studied the structural transformation of the high-chirality LC under uniaxial deformation using mean field simulations. As was shown before, consistent with the experimental observation, the high-chirality LC confined into an oblate spheroid ($D_x = D_y$) forms a DOS and exhibits a topological line defect that makes a knot. This unique structure appears as a curly and symmetric ring in the simulated cross-polarizer images when the system is observed from the *z* axis (optical axis) (Figs. 2F and 4C). Upon uniaxial deformation, however, the high-chirality LC adopts a deformed RSS configuration with cholesteric layers that are no longer flat and instead show oscillations (Fig. 4D). At the central region of the deformed droplet, the stretching induces a director alignment that lies on the *xy* plane (blue region, Fig. 4E); i.e., the LC tends to adopt a uniform configuration—as expected in nematic LCs—and the helical rotation is mainly presented along the *z* axis. Localized zones of high bend and splay deformation are also formed at the central region where the director rotates, which are identified by the isosurfaces of splay (blue) and bend (yellow) order parameter (fig. S5); at these regions, we observe changes in the wavelength of the reflected light. The corresponding cross-polarized images have a texture that is similar to those observed in our experiments (Fig. 4C).

We further investigated the optical properties of the BP structures in a confined ellipsoidal geometry. Upon increasing the temperature, the cross-polarized micrographs and reflection wavelengths demonstrate phase transitions from cholesteric (25°) to BPI (42.5°C), then to BPII (43.9°C), and eventually to isotropic (45°C) (Fig. 5, A and B). Interestingly, analysis of images of the BP reveals two distinct regions in the ellipsoidal domain, in which the outer part of the stretched droplet exhibits BP characteristics (BPI at 42.5°C and BPII at 43.9°C) (Fig. 5, A and B) at a lower temperature compared to the inner core. This can be attributed to the possible structural alteration of the disclination lines of blue phases induced by geometrical confinement.

To better understand the influence of the confined geometry on the BP structures of the high-chirality LC, we turned to continuum simulations of blue phases confined into geometries provided by our experiments, with planar anchoring conditions. These calculations reveal changes in the BP-lattice periodicity that are induced by the interfacial strain (Fig. 5, C and D). Specifically, we analyzed three geometries with spatial dimensions: G1: $D_x = D_y = 2D_z$; G2:

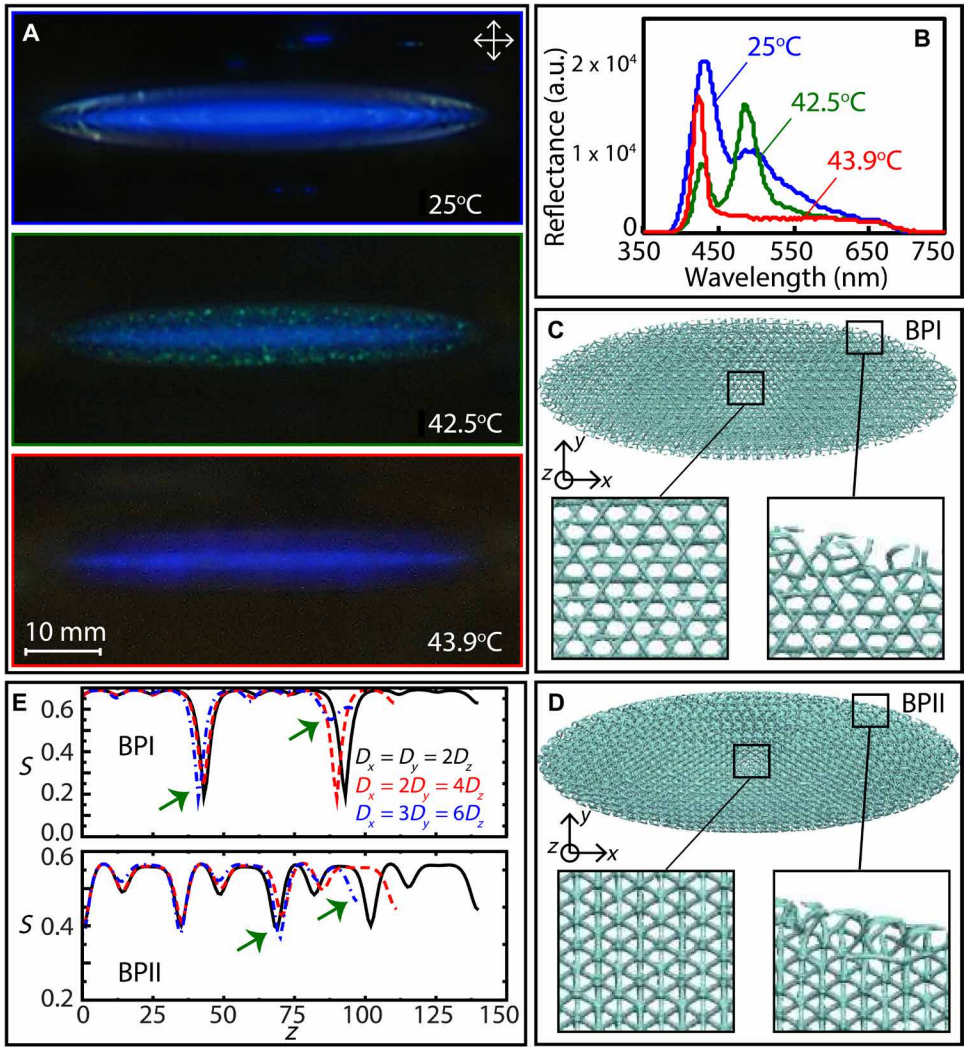

Fig. 5. BP transitions in an initially deformed highly chirality droplet. (**A**) Cross-polarized reflection mode micrographs of a stretched high-chirality LC droplet ($\varepsilon = 2.5$) at different phases: cholesteric, BPI, and BPII. (**B**) Measured reflectance spectra of the stretched high-chirality LC droplet in different phases: cholesteric, BPI, and BPII. Snapshots along the *z* axis of the simulated defect structure of a uniaxially stretched (**C**) BPI and (**D**) BPII, from an initial oblate geometry to $x = 3y$. (**E**) Scalar order parameter along the *z* axis for BPI and BPII, respectively. The scalar order parameter of the initial oblate-like geometry (solid black line) has been compared with two representative stretched geometries (red and blue dashed lines).

$D_x = 2D_y = 4D_z$; and G3: $D_x = 3D_y = 6D_z$ (D_x, D_y, and D_z are the droplet lengths in the *x*, *y*, and *z* directions, respectively). In all cases, we extracted the behavior of the scalar order parameter, *S*, along the *x*, *y*, and *z* axes. Since *S* drops off in the vicinity of the disclination lines, this parameter can be used to detect possible changes in the periodicity of the BPs (*21*). We find that, at the core of the systems, both BPI and BPII do not present visible changes of lattice periodicity; i.e., they exhibit a bulk-like structure. As the material approaches the interface, the unit cells shrink, producing a change in the periodicity of the material. Figure 5E shows *S*, for BPI and BPII, as a function of z^*, where $z = \xi z^*$ and $\xi = 7.5$ nm is the coherence length. The center of the system is at $(x^*, y^*, z^*) = (0, 0, 0)$; the results for x^* and y^* dependence are shown in the Supplementary Materials (fig. S6). For G1, $D_z = 284$ $\xi = 2130$ nm; for G2, $D_z = 221$ $\xi = 1657.5$ nm; and for G3, $D_z = 194$ $\xi = 1455$ nm. Therefore, changes in the lattice periodicity along the *z* axis are seen first in G3, then in G2, and last in G1. Our simulations also show that, at the interface, the (110) lattice orientation is the preferred orientation for BPI, and for BPII, it is (111); thus, the BPI shows a green color at the interface, and it is dark for BPII. In the experiments, the blue color of the BPII comes from light reflected from the (100) planes, but it is dark at the interfaces, which is consistent with our simulation results.

CONCLUSIONS

Experimental studies and computational simulations have been used to elucidate the effects of mechanical strain and nonspherical geometrical confinement on the molecular organization and optical properties of chiral LCs. Two polymers (PVA and PAA) were used to create a matrix in which chiral LC droplets were embedded, both of which promote strong planar anchoring of the LC. Upon biaxial compression and uniaxial extension, LC droplets deform into oblate and ellipsoidal droplets, respectively. When the chiral LC is forced into an oblate geometry, the droplet exhibits two regions with distinct

molecular alignments. While the outer part maintains RSS features, with a randomly oriented helical axis, the inner part adopts a disc-shape topology, with the LC helix aligned normal to the surface that selectively reflects light of a color corresponding to the pitch length.

We have found that uniaxial deformation of the chiral LC droplets destabilizes the RSS configuration and induces the formation of helical structures. Upon increasing the temperature, the high-chirality LC confined into ellipsoidal domains reveals two distinct regions (core-shell) in the BP configuration space, where the BP characteristics for the outer shell appear at a lower temperature.

Overall, these findings indicate that the coupling of mechanical strain, curvature, and elasticity of the chiral LC leads to the emergence of completely new molecular configurations that can be stabilized by deformation, paving the way for applications that include mechano-optical metamaterials, smart coatings, and wearable electronic devices.

SUPPLEMENTARY MATERIALS

Supplementary material for this article is available at http://advances.sciencemag.org/cgi/content/full/6/28/eaba6728/DC1

REFERENCES AND NOTES

1. S. Klein, Electrophoretic LC displays: How far are we? *Liq. Cryst. Rev.* **1**, 52–64 (2013).
2. F. Peng, F. Gou, H. Chen, Y. Huang, S.-T. Wu, A submillisecond-response liquid crystal for color sequential projection displays. *J. Soc. Inf. Disp.* **24**, 241–245 (2016).
3. Y. Takane, Y. Kawasumi, M. Sato, T. Horie, T. Ishibashi, Evaluating clinical implications of 15-mega-sub-pixel liquid-crystal display in phase-contrast mammography. *Breast Cancer* **23**, 561–567 (2016).
4. P. S. Drzaic, *Liquid Crystal Dispersions* (World Scientific Publishing Co., 1995), vol. 1.
5. I.-H. Lin, D. S. Miller, P. J. Bertics, C. J. Murphy, J. J. de Pablo, N. L. Abbott, Endotoxin-induced structural transformations in liquid crystalline droplets. *Science* **332**, 1297–1300 (2011).
6. M. Sadati, A. I. Apik, J. C. Armas-Perez, J. Martinez-Gonzalez, J. P. Hernandez-Ortiz, N. L. Abbott, J. J. de Pablo, Liquid crystal enabled early stage detection of beta amyloid formation on lipid monolayers. *Adv. Funct. Mater.* **25**, 6050–6060 (2015).
7. H. Ramezani-Dakhel, M. Sadati, M. Rahimi, A. Ramirez-Hernandez, B. Roux, J. J. de Pablo, Understanding atomic-scale behavior of liquid crystals at aqueous interfaces. *J. Chem. Theory Comput.* **13**, 237–244 (2017).
8. M. Sadati, H. Ramezani-Dakhel, W. Bu, E. Sevgen, Z. Liang, C. Erol, M. Rahimi, N. T. Qazvin, B. H. Lin, N. L. Abbott, B. Roux, M. L. Schlossman, J. J. de Pablo, Molecular structure of canonical liquid crystal interfaces. *J. Am. Chem. Soc.* **139**, 3841–3850 (2017).
9. L. Wang, Q. Li, Stimuli-directing self-organized 3D liquid-crystalline nanostructures: From materials design to photonic applications. *Adv. Funct. Mater.* **26**, 10–28 (2016).
10. J. Noh, H. L. Liang, I. Drevensek-Olenik, J. P. F. Lagerwall, Tuneable multicoloured patterns from photonic cross-communication between cholesteric liquid crystal droplets. *J. Mater. Chem. C* **2**, 806–810 (2014).
11. S. J. Asshoff, S. Sukas, T. Yamaguchi, C. A. Hommersom, S. Le Gac, N. Katsonis, Superstructures of chiral nematic microspheres as all-optical switchable distributors of light. *Sci. Rep.* **5**, 14183 (2015).
12. F. Xu, P. P. Crooker, Chiral nematic droplets with parallel surface anchoring. *Phys. Rev. E* **56**, 6853–6860 (1997).
13. C. B. Heinz Kitzerow, *Chirality in Liquid Crystals* (Springer-Verlag New York, 2001).
14. J. A. Martinez-Gonzalez, X. Li, M. Sadati, Y. Zhou, R. Zhang, P. F. Nealey, J. J. de Pablo, Directed self-assembly of liquid crystalline blue-phases into ideal single-crystals. *Nat. Commun.* **8**, 15854 (2017).
15. X. Li, J. A. Martinez-Gonzalez, J. P. Hernandez-Ortiza, A. Ramirez-Hernandez, Y. Zhou, M. Sadati, R. Zhang, P. F. Nealey, J. J. de Pablo, Mesoscale martensitic transformation in single crystals of topological defects. *Proc. Natl. Acad. Sci. U.S.A.* **114**, 10011–10016 (2017).
16. D. C. Wright, N. D. Mermin, Crystalline liquids: The blue phases. *Rev. Mod. Phys.* **61**, 385–432 (1989).
17. P. P. Crooker, The cholesteric blue phase: A progress report. *Mol. Cryst. Liq. Cryst.* **98**, 31–45 (1983).
18. J.-i. Fukuda, S. Zumer, Novel defect structures in a strongly confined liquid-crystalline blue phase. *Phys. Rev. Lett.* **104**, 017801 (2010).
19. J. Fukuda, S. Zumer, Quasi-two-dimensional skyrmion lattices in a chiral nematic liquid crystal. *Nat. Commun.* **2**, 246 (2011).
20. J. Fukuda, S. Zumer, Ring defects in a strongly confined chiral liquid crystal. *Phys. Rev. Lett.* **106**, 097801 (2011).
21. J. A. Martinez-Gonzalez, Y. Zhou, M. Rahimi, E. Bukusoglu, N. L. Abbott, J. J. de Pablo, Blue-phase liquid crystal droplets. *Proc. Natl. Acad. Sci. U.S.A.* **112**, 13195–13200 (2015).
22. J. Fukuda, S. Zumer, Structural forces in liquid crystalline blue phases. *Phys. Rev. E* **84**, 040701 (2011).
23. M. Urbanski, C. G. Reyes, J. Noh, A. Sharma, Y. Geng, V. S. R. Jampani, J. P. Lagerwall, Liquid crystals in micron-scale droplets, shells and fibers. *J. Phys. Condens. Matter* **13**, 29 (2017).
24. P. J. Ackerman, I. I. Smalyukh, Reversal of helicoidal twist handedness near point defects of confined chiral liquid crystals. *Phys. Rev. E* **93**, 052702 (2016).
25. G. Posnjak, *Topological Formations in Chiral Nematic Droplets* (Springer, 2018).
26. S. Afghah, J. V. Selinger, Theory of helicoids and skyrmions in confined cholesteric liquid crystals. *Phys. Rev. E* **96**, 012708 (2017).
27. M. Humar, I. Musevic, 3D microlasers from self-assembled cholesteric liquid-crystal microdroplets. *Opt. Express* **18**, 26995–27003 (2010).
28. D. Sec, T. Porenta, M. Ravnik, S. Zumer, Geometrical frustration of chiral ordering in cholesteric droplets. *Soft Matter* **8**, 11982–11988 (2012).
29. T. Orlova, S. J. Asshoff, T. Yamaguchi, N. Katsonis, E. Brasselet, Creation and manipulation of topological states in chiral nematic microspheres. *Nat. Commun.* **6**, 7603 (2015).
30. J. Yoshioka, F. Ito, Y. Suzuki, H. Takahashi, H. Takizawa, Y. Tabe, Director/barycentric rotation in cholesteric droplets under temperature gradient. *Soft Matter* **10**, 5869–5877 (2014).
31. M. N. Krakhalev, A. P. Gardymova, O. O. Prishchepa, V. Y. Rudyak, A. V. Emelyanenko, J. H. Liu, V. Y. Zyryanov, Bipolar configuration with twisted loop defect in chiral nematic droplets under homeotropic surface anchoring. *Sci. Rep.* **7**, 14587 (2017).
32. Y. Zhou, E. Bukusoglu, J. A. Martinez-Gonzalez, M. Rahimi, T. F. Roberts, R. Zhang, X. G. Wang, N. L. Abbott, J. J. de Pablo, Structural transitions in cholesteric liquid crystal droplets. *ACS Nano* **10**, 6484–6490 (2016).
33. E. Bukusoglu, X. G. Wang, Y. Zhou, J. A. Martinez-Gonzalez, M. Rahimi, Q. Wang, J. J. de Pablo, N. L. Abbott, Positioning colloids at the surfaces of cholesteric liquid crystal droplets. *Soft Matter* **12**, 8781–8789 (2016).
34. S. S. Lee, S. K. Kim, J. C. Won, Y. H. Kim, S. H. Kim, Reconfigurable photonic capsules containing cholesteric liquid crystals with planar alignment. *Angew. Chem. Int. Ed.* **54**, 15266–15270 (2015).
35. M. Bagnani, P. Azzari, S. Assenza, R. Mezzenga, Six-fold director field configuration in amyloid nematic and cholesteric phases. *Sci. Rep.* **9**, 12654 (2019).
36. E. Bukusoglu, X. G. Wang, J. A. Martinez-Gonzalez, J. J. de Pablo, N. L. Abbott, Stimuli-responsive cubosomes formed from blue phase liquid crystals. *Adv. Mater.* **27**, 6892–6898 (2015).
37. V. Palacio-Betancur, J. C. Armas-Perez, S. Villada-Gil, N. L. Abbott, J. P. Herna´ndez-Ortiz, J. J. de Pablo, Cuboidal liquid crystal phases under multiaxial geometrical frustration. *Soft Matter* **16**, 870 (2020).
38. A. Darmon, O. Dauchot, T. Lopez-Leon, M. Benzaquen, Elastic interactions between topological defects in chiral nematic shells. *Phys. Rev. E* **94**, 062701 (2016).
39. A. Darmon, M. Benzaquen, D. Sec, S. Copar, O. Dauchot, T. Lopez-Leon, Waltzing route toward double-helix formation in cholesteric shells. *Proc. Natl. Acad. Sci. U.S.A.* **113**, 9469–9474 (2016).
40. M. O. L. Lisa Tran, G. Durey, A. Darmon, M. F. Haase, N. Li, D. Lee, K. J. Stebe, R. D. Kamien, T. Lopez-Leon, Change in stripes for cholesteric shells via anchoring in moderation. . *Rev. X* **7**, 041029 (2017).
41. S. S. Lee, H. J. Seo, Y. H. Kim, S. H. Kim, Structural color palettes of core-shell photonic ink capsules containing cholesteric liquid crystals. *Adv. Mater.* **29**, 1606894 (2017).
42. Y. Zhou, A. Guo, R. Zhang, J. C. Armas-Perez, J. A. Martinez-Gonzalez, M. Rahimi, M. Sadati, J. J. de Pablo, Mesoscale structure of chiral nematic shells. *Soft Matter* **12**, 8983–8989 (2016).
43. M. Schwartz, G. Lenzini, Y. Geng, P. B. Rønne, P. Y. A. Ryan, J. P. F. Lagerwall, Cholesteric liquid crystal shells as enabling material for information-rich design and architecture. *Adv. Mater.* **30**, 1707382 (2018).
44. Y. Geng, J.-H. Jang, K.-G. Noh, J. Noh, J. P. F. Lagerwall, S.-Y. Park, Through the spherical looking-glass: Asymmetry enables multicolored internal reflection in cholesteric liquid cystal shells. *Adv. Opt. Mater.* **6**, 1700923 (2018).
45. S. S. Lee, S.-H. Kim, Controlled encapsulation of cholesteric liquid crystals using emulsion templates. *Macromol. Res.* **26**, 1054 (2018).
46. A. R. Fialho, N. R. Bernardino, N. M. Silvestre, M. M. Telo da Gama, Effect of curvature on cholesteric liquid crystals in toroidal geometries. *Phys. Rev. E* **96**, 012702 (2017).
47. C. R. Wand, M. A. Bates, Chiral nematic liquid crystals in torus-shaped and cylindrical cavities. *Phys. Rev. E* **100**, 052702 (2019).
48. G. P. Alexander, J. M. Yeomans, Numerical results for blue phases. *Liq. Cryst.* **36**, 1215–1227 (2009).

49. M. Ravnik, S. Žumer, Landau–de Gennes modeling of nematic liquid crystal colloids. *Liq. Cryst.* **36**, 1201–1214 (2009).
50. V. Tomar, S. I. Hernandez, N. L. Abbott, J. P. Hernandez-Ortiz, J. J. de Pablo, Morphological transitions in liquid crystal nanodroplets. *Soft Matter* **8**, 8679–8689 (2012).
51. A. Dupuis, D. Marenduzzo, J. M. Yeomans, Numerical calculations of the phase diagram of cubic blue phases in cholesteric liquid crystals. *Phys. Rev. E* **71**, 011703 (2005).
52. J. Bezic, S. Žumer, Structures of the cholesteric liquid crystal droplets with parallel surface anchoring. *Liq. Cryst.* **11**, 593–619 (1992).
53. D. J. Gardiner, S. M. Morris, P. J. W. Hands, C. Mowatt, R. Rutledge, T. D. Wilkinson, H. J. Coles, Paintable band-edge liquid crystal lasers. *Opt. Express* **19**, 2432–2439 (2011).
54. D. Sec, T. Lopez-Leon, M. Nobili, C. Blanc, A. Fernandez-Nieves, M. Ravnik, S. Žumer, Defect trajectories in nematic shells: Role of elastic anisotropy and thickness heterogeneity. *Phys. Rev. E* **86**, 020705 (2012).
55. D. Rolfsen, *Knots and Links* (Publish or Perish Inc., 1976).
56. P. V. Shibaev, P. Rivera, D. Teter, S. Marsico, M. Sanzari, V. Ramakrishnan, E. Hanelt, Color changing and lasing stretchable cholesteric films. *Opt. Express* **16**, 2965–2970 (2008).
57. P. V. Shibaev, R. Uhrlass, S. Woodward, C. Schlesier, M. R. Ali, E. Hanelt, Mechanism of colour changes in stretchable cholesteric films. *Liq. Cryst.* **37**, 587–592 (2010).
58. G. Kamita, B. Frka-Petesic, A. Allard, M. Dargaud, K. King, A. G. Dumanli, S. Vignolini, Biocompatible and sustainable optical strain sensors for large-area applications. *Adv. Opt. Mater.* **4**, 1950–1954 (2016).
59. F. Castles, S. M. Morris, J. M. C. Hung, M. M. Qasim, A. D. Wright, S. Nosheen, S. S. Choi, B. I. Outram, S. J. Elston, C. Burgess, L. Hill, T. D. Wilkinson, H. J. Coles, Stretchable liquid-crystal blue-phase gels. *Nat. Mater.* **13**, 817–821 (2014).
60. M. Mitani, S. Ogata, S. Yamane, M. Yoshio, M. Hasegawab, T. Kato, Mechanoresponsive liquid crystals exhibiting reversible luminescent color changes at ambient temperature. *J. Mater. Chem. C* **4**, 2752–2760 (2016).

Acknowledgments

Funding: This work was supported by the Department of Energy, Office of Basic Energy Sciences, Division of Materials Science and Engineering, under grant DE-SC0019762. The calculations presented in this work were carried out on the GPU cluster at the University of Chicago, supported by the National Science Foundation under MRI grant 1828629. J.A.M.-G. acknowledges computer resources, technical advice, and support provided by the Laboratorio Nacional de Supercómputo del Sureste de México (LNS), a member of the CONACYT national laboratories, with project no. 201901023N. **Author contributions:** M.S. and J.J.d.P. conceived the experiments, and M.S. performed them. J.A.M.-G., Y.Z., and J.J.d.P. conceived and performed numerical simulations and theoretical calculations. M.S., J.A.M.-G., Y.Z., and J.J.d.P. wrote the manuscript. J.J.d.P. guided the work. N.T.Q. contributed to setting up the heating system for phase transition measurements of the stretched samples and performing Scanning Electron Microscopy. X.L. contributed to the electric field setup. K.K. contributed to optical observation of the deformed samples. R.Z. and J.P.H. contributed to analysis and interpretation of the theoretical results. E.B. and N.L.A. contributed to analysis and interpretation of the experimental results. **Competing interests:** The authors declare that they have no competing interests. **Data and materials availability:** All data needed to evaluate the conclusions in the paper are present in the paper and/or the Supplementary Materials. Additional data related to this paper may be requested from the authors.

Submitted 21 December 2019
Accepted 28 May 2020
Published 10 July 2020
10.1126/sciadv.aba6728

Citation: M. Sadati, J. A. Martinez-Gonzalez, Y. Zhou, N. T. Qazvini, K. Kurtenbach, X. Li, E. Bukusoglu, R. Zhang, N. L. Abbott, J. P. Hernandez-Ortiz, J. J. de Pablo, Prolate and oblate chiral liquid crystal spheroids. *Sci. Adv.* **6**, eaba6728 (2020).

Science Advances

Prolate and oblate chiral liquid crystal spheroids

Monirosadat Sadati, Jose A. Martinez-Gonzalez, Ye Zhou, Nader Taheri Qazvini, Khia Kurtenbach, Xiao Li, Emre Bukusoglu, Rui Zhang, Nicholas L. Abbott, Juan Pablo Hernandez-Ortiz and Juan J. de Pablo

Sci Adv **6** (28), eaba6728.
DOI: 10.1126/sciadv.aba6728

Science Advances (ISSN 2375-2548) is published by the American Association for the Advancement of Science, 1200 New York Avenue NW, Washington, DC 20005. The title *Science Advances* is a registered trademark of AAAS.